Chemical Science

ROYAL SOCIETY OF CHEMISTRY

EDGE ARTICLE

View Article Online
View Journal | View Issue

Check for updates

Cite this: *Chem. Sci.*, 2024, **15**, 12989

All publication charges for this article have been paid for by the Royal Society of Chemistry

Orbital electron delocalization of axial-coordinated modified FeN_4 and structurally ordered PtFe intermetallic synergistically for efficient oxygen reduction reaction catalysis†

Chenzhong Wu, Meida Chen, Bin Wang, Leqing Luo, Qian Zhou, Guangtao Mao, Yuan Xiong and Qingmei Wang *

Regulating the chemical environment of materials to optimize their electronic structure, leading to the optimal adsorption energies of intermediates, is of paramount importance to improving the performance of electrocatalysts, yet remains an immense challenge. Herein, we design a harmonious axial-coordination Pt_xFe/FeN_4CCl catalyst that integrates a structurally ordered PtFe intermetallic with an orbital electron-delocalization FeN_4CCl support for synergistically efficient oxygen reduction catalysis. The obtained Pt_2Fe/FeN_4CCl with a favorable atomic arrangement and surface composition exhibits enhanced oxygen reduction reaction (ORR) intrinsic activity and durability, achieving a mass activity (MA) and specific activity (SA) of 1.637 A mg_{Pt}^{-1} and 2.270 mA cm^{-2}, respectively. Detailed X-ray absorption fine spectroscopy (XAFS) further confirms the axial-coupling effect of the FeN_4CCl substrate by configuring the Fe–N bond to ~1.92 Å and the Fe–Cl bond to ~2.06 Å. Additionally, Fourier transforms of the extended X-ray absorption fine structure (FT-EXAFS) demonstrate relatively prominent peaks at ~1.5 Å, ascribed to the contribution of the Fe–N/Fe–Cl, further indicating the construction of the FeN_4CCl moiety structure. More importantly, the electron localization function (ELF) and density functional theory (DFT) further determine an orbital electron delocalization effect due to the strong axial traction between the Cl atoms and FeN_4, resulting in electron redistribution and modification of the coordination surroundings, thus optimizing the adsorption free energy of OH_{abs} intermediates and effectively accelerating the ORR catalytic kinetic process.

Received 27th April 2024
Accepted 7th July 2024

DOI: 10.1039/d4sc02824d

rsc.li/chemical-science

Open Access Article. Published on 08 July 2024. Downloaded on 4/2/2026 6:00:46 PM.
This article is licensed under a Creative Commons Attribution-NonCommercial 3.0 Unported Licence.

1. Introduction

Proton exchange membrane fuel cells (PEMFCs) as a potential clean energy-efficient conversion technique have gained extensive attention owing to their characteristics of being environmentally friendly and high-efficiency as power sources for a variety of transportation systems, especially mid-size and heavy-duty vehicles and light railway transits.[1,2] For large-scale applications, a key developmental target for these PEMFCs is to reduce the extensive use of precious platinum in the Pt-based nanocatalysts.[3] At present, the consumption of Pt in fuel cell stacks has decreased to 0.3–0.4 g_{Pt} kW^{-1}, but there is still a considerable gap from the requirements of fuel cell vehicle industrialization (<0.1 g_{Pt} kW^{-1}).[4,5] To fulfil this purpose, researchers have focused on the following: (1) developing a catalyst with optimized coordination circumstances to modify the electron structure of Pt and the adsorption energy of intermediates to accelerate the oxygen reduction reaction (ORR) kinetics; (2) designing a catalyst with a structurally ordered phase for eliminating the dissolution of less-noble metals at the atomic scale observed in the disordered counterpart; (3) conceiving a highly stable support to enhance the bond length to resist the corrosion of the carrier and ensure accessibility of sites to maximize Pt utilization.[6–8]

For simultaneously realizing the enhancement of the mass activities and stability in fuel cells, great efforts towards the development of such advanced Pt-based catalysts have been dedicated.[9,10] Among them, the carbon-supported Pt-based alloy materials have gained tremendous attention because of the rapid ORR kinetics in acidic media, but they are not yet durable enough for practical commercial applications owing to the carbon corrosion during potential cycling.[11,12] Supported structurally ordered Pt-based electrocatalysts with a determined atomic arrangement and a surface composition that consists of a transition metal atomically dispersed in a nitrogen-coordinated

Guizhou University Key Laboratory of Green Chemical and Clean Energy Technology, Guizhou University Engineering Research Center of Efficient Utilization for Industrial Waste, Institute of Dual-carbon and New Energy Technology Innovation and Development of Guizhou Province, School of Chemistry and Chemical Engineering, Guizhou University, Guiyang 550025, China. E-mail: qmwang3@gzu.edu.cn

† Electronic supplementary information (ESI) available. See DOI: https://doi.org/10.1039/d4sc02824d

© 2024 The Author(s). Published by the Royal Society of Chemistry

Open Access Article. Published on 08 July 2024. Downloaded on 4/2/2026 6:00:46 PM. This article is licensed under a Creative Commons Attribution-NonCommercial 3.0 Unported Licence.

carbon (M–N–C, M = Fe, Co, Ni, Mn, *etc.*) support and structurally ordered phase have emerged as promising candidates with improved durability and mass activity towards the ORR.[13,14] Unfortunately, the N atom in M–N–C is attacked by protons generated during the reduction reaction ($M–N + H_2O \rightarrow M(OH)_2 + (NH)_2$), leading to the breaking of the M–N bond and the continuous dissolution of the metal from the single atom active center of M, seriously affecting the activity of the catalyst.[15,16] Hence, considerable effort has been devoted to addressing the above problems, with efforts concentrated, in part, on retouching the coordination environment and the chemical composition of M–N–C.[17,18] Previous DFT calculations have proven that the configuration coordination environment of M–N–C can determine the electronic structure of Pt and M, which remarkedly affects the adsorption free energy of the oxygen species ($O_{2,abs}$, $H_2O_{2,abs}$, OH_{abs} and OOH_{abs}) on the Pt center and thus gives rise to variations in the ORR intrinsic activity.[19,20] Thus, in this direction, a catalyst with an optimized coordination state for active Pt sites and a heterogeneous local environment for the M–N–C must be rationally designed and engineered.

Herein, we successfully synthesize a concordant Pt_xFe/FeN_4-CCl catalyst that combines the axial-coordinated modified FeN_4 of an orbital electron delocalization effect with structurally ordered PtFe intermetallic for synergistically highly efficient ORR. The unique structure of the catalyst was fabricated by a pyrolysis reduction strategy at high-temperature conditions (Scheme S1†), in which Fe in the hemin precursor alloys with Pt atoms and forms axial-coordinated modified Fe single-atoms. X-ray adsorption fine spectroscopy (XAFS) analyses reveal that a Fe atom coordinates with one axial Cl atom and four N atoms, effectively authenticating the structure of the three-dimensional FeN_4CCl architectures. The orbital electron delocalization of chlorine-coordinated modified FeN_4 in the FeN_4CCl support was confirmed by configuring the Fe–N bond for ∼1.92 Å and Fe–Cl bond for ∼2.06 Å. Additionally, DFT calculations proclaimed that the $PtFe/FeN_4CCl$ shows the lowest adsorption free energy of OH_{abs} species ($E_{OH_{abs}} = 2.51$ eV) relative to FeN_4C ($E_{OH_{abs}} = 3.07$ eV), FeN_4CCl ($E_{OH_{abs}} = 2.75$ eV), and PtFe ($E_{OH_{abs}} = 3.25$ eV). This is attributed to the electron redistribution and modification of the coordination surroundings, resulting from a strong axial traction effect between the Cl atoms and FeN_4. Benefiting from the chlorine-coordinated modified FeN_4CCl support and the synergistic catalysis with the structurally ordered PtFe intermetallic, the obtained Pt_2Fe/FeN_4CCl catalyst with optimum surface composition exhibits a higher MA of 1.637 A mg_{Pt}^{-1} and SA of 2.270 mA cm^{-2}, respectively, surpassing the commercial Pt/C catalyst (0.165 A mg_{Pt}^{-1} and 0.264 mA cm^{-2}). Therefore, our work gives significant insight into designing high-performance electrocatalysts with synergistic catalysis by combining tailored axial-coordinated modified non-precious metal active sites with a structurally ordered Pt-based intermetallic.

2. Results and discussion

2.1 Morphology and structure characterization

The structures and crystallinity properties of the Pt_xFe/FeN_4CCl samples and commercial Pt/C were characterized by powder X-ray diffraction (PXRD), where X represents the weight ratio of Pt to contained Fe in the hemin precursor ($X = 1$, 2, and 3, respectively; more detailed information is given in the ESI†). All the characteristic diffraction peaks of the Pt_xFe/FeN_4CCl sample exhibit a slight positive shift to higher angles compared with the commercial Pt/C catalyst (PDF#04-0802), suggesting that the alloy phase has been attained by the introduction of smaller Fe atoms (Fig. 1a).[21] Importantly, the ordered characteristic peaks at 2θ of 23.93° for the (001) plane, 33.90° for the (110) plane, and 41.07° for the (111) plane were further observed in the Pt_xFe/FeN_4CCl sample, indicating the formation of structurally ordered PtFe intermetallic (PDF#43-1359).[22,23] In addition, the ordered degree of all as-prepared catalysts was determined by calculating the peak intensity ratio of the characteristic planes (110) and (111), which demonstrated that Pt_2Fe/FeN_4CCl (0.275) shows a higher ordered degree than Pt_1Fe/FeN_4CCl (0.233) and Pt_3Fe/FeN_4CCl (0.266) (Table S1†).[24,25] The Pt_2Fe/FeN_4CCl catalyst with a higher ordered degree and favorable surface composition was synthesized by precisely manipulating the feeding weight ratio of Pt to the contained Fe^{2+} precursor. The shape and structure of the as-prepared Pt_2Fe/FeN_4CCl materials were further investigated by transmission electron microscopy (TEM), aberration-corrected high-angle annular dark field scanning transmission electron microscopy (AC-HAADF-STEM), and X-ray energy dispersive spectroscopy (EDS). The overall TEM images of the Pt_2Fe/FN_4CCl catalysts and their corresponding particle diameter histograms are presented in Fig. 1b and c, exhibiting nanoparticles uniformly distributed throughout the whole support, with an average edge length of 3.38 ± 0.2 nm. AC-HAADF-STEM analyses were performed to further characterize the catalyst structure and surface composition. As displayed in Fig. 1d, we can observe that abundant bright isolated dots are regularly scattered in the modified graphitic carbon matrix, which are attributed to Fe single atoms, indicating that Fe single sites co-coordinated with chlorine-nitrogen and embedded in carbon (Fe–N–C–Cl) were formed. Besides, as presented in Fig. 1e–h, the high-resolution TEM images of the Pt_2Fe/FeN_4CCl sample reveal the as-prepared catalyst nanoparticle composition of an ordered PtFe alloy phase and an Fe single atom substrate, further verifying that a multiple-structure catalyst has been triumphantly synthesized. The corresponding fast Fourier transform (FFT) further measures the lattice fringes with *d*-spacings of 0.183 nm for the characteristic planes of the (110) facet and 0.227 nm for the (111) facet, which is consistent with the XRD results. Meanwhile, the corresponding line scan profile analysis of the area of line 1 and line 2 displayed the formation of ordered PtFe intermetallic *via* the incorporation of smaller Fe atoms into the Pt crystal lattice.[26] Moreover, as shown in Fig. 1i, EDS element mapping images of Pt_2Fe/FeN_4CCl indicate that Pt atoms are primarily centralized on the whole ordered PtFe intermetallic. However, some Fe atoms manufacture the ordered intermetallic and others are allocated to generate single-atoms, demonstrating that the synergistic catalyst consists of an ordered PtFe intermetallic and Fe single-atom support. Furthermore, the atomic ratio of Pt/Fe is estimated as 32/68, confirmed by electron energy loss spectroscopy (EELS) (Fig. 1j), the EDS spectrum

© 2024 The Author(s). Published by the Royal Society of Chemistry

Open Access Article. Published on 08 July 2024. Downloaded on 4/2/2026 6:00:46 PM.
This article is licensed under a Creative Commons Attribution-NonCommercial 3.0 Unported Licence.

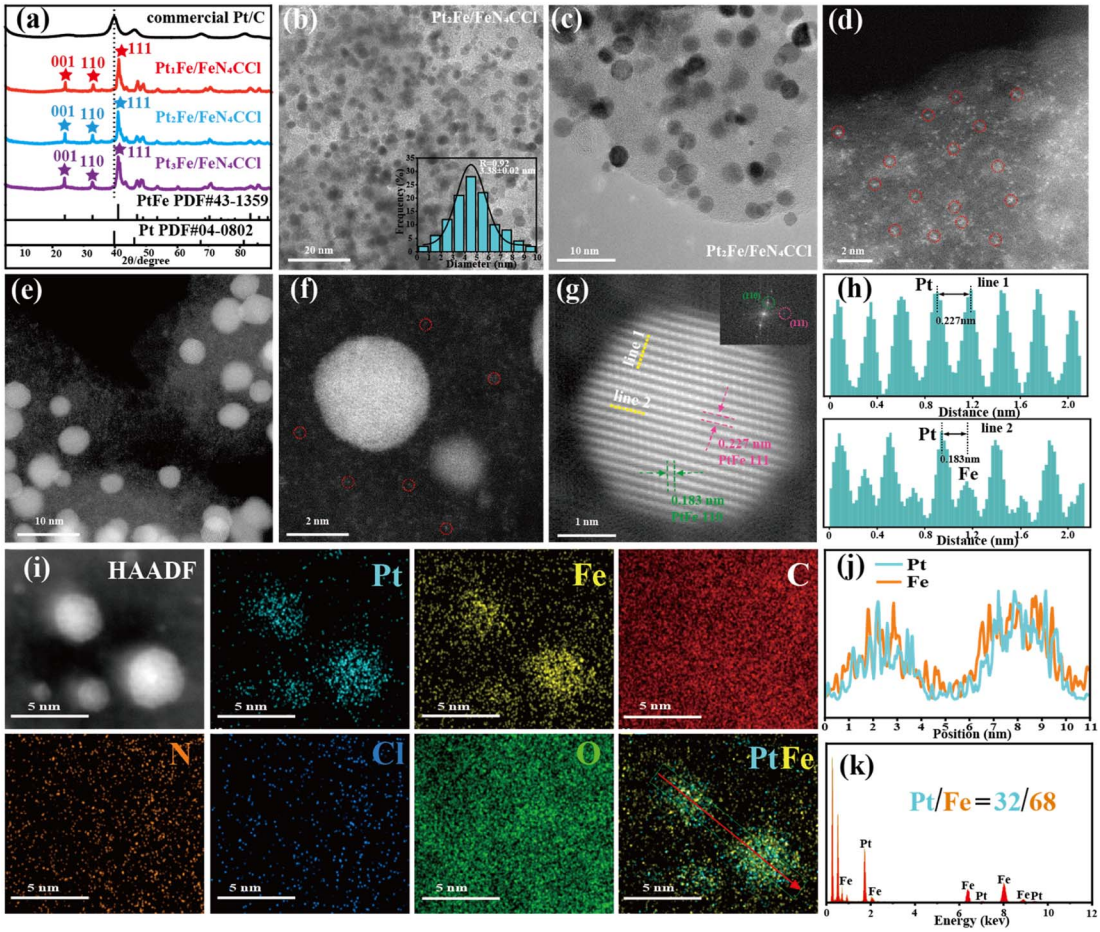

Fig. 1 (a) XRD patterns of the commercial Pt/C, Pt_1Fe/FeN_4CCl, Pt_2Fe/FeN_4CCl, and Pt_3Fe/FeN_4CCl samples. (b and c) TEM and the corresponding particle size distribution images of Pt_2Fe/FeN_4CCl. (d and e) AC-HAADF-TEM images of the Pt_2Fe/FeN_4CCl sample and a single particle. (f and g) HR-TEM and the corresponding FFT images in the Pt_2Fe/FeN_4CCl sample and (h) the corresponding line scan profiles marked in g, corresponding with the area of line 1 (top) showing only Pt atoms as well as line 2 between Pt and Fe atoms (bottom). (i) HAADF-STEM images of the Pt_2Fe/FeN_4CCl sample and corresponding elemental mapping image. (j) EELS profile. (k) EDS spectrum of the corresponding element mapping.

(Fig. 1k), and inductively coupled plasma optical emission spectrometry (ICP-OES) analysis (Table S2†). Simultaneously, the element of Cl was also detected in the Pt_2Fe/FeN_4CCl catalyst, indicating that the Cl atoms of the hemin precursor have been successfully transformed into the axial-ligand of the coordinated modified FeN_4CCl substrate.

X-ray adsorption fine spectroscopy (XAFS) analysis was carried out to further analyze the local coordination environment and electronic structure at the atomic level. The Pt L_3-edge X-ray absorption near-edge structure (XANES) spectra of Pt_2Fe/FeN_4CCl with Pt foil and PtO_2 as references are shown in Fig. 2a.[27] The XANES of the white line intensity (~11 569 eV), edge energy, and shapes in the Pt_2Fe/FeN_4CCl catalyst are similar to those of Pt foil, suggesting that the chemical states are approximately zero-valence. Previous studies have proven that a higher content of Pt (0) in the alloy catalysts is beneficial to improving the ORR catalytic kinetics.[28] Additionally, the Fourier transforms of the extended X-ray absorption fine structure (FT-EXAFS) spectra (Fig. 2b) demonstrate that the relatively prominent peak at ~1.5 Å should be assigned to Pt–N bonds, declaring the strong metal-support interaction.[29,30] Moreover, due to heteroatomic interactions in Pt–Fe alloying, a shorter radial distance in comparison to that of Pt foil is ascribed to the contribution of the Pt–Pt/Pt–Fe bond at ~2.63 Å, further indicating the construction of a PtFe intermetallic interface.[31] Compared with the *R*, *k* and *q* space diagrams of Pt foil and PtO_2 (Fig. S1†), the fitting information presented in Fig. 2c for Pt_2Fe/FeN_4CCl further supports that the Pt–Pt bond length is shortened to induce a compressive effect due to the PtFe alloy formation. The scattering peak at ~1.5 Å is from the contribution of Pt–N bonds, suggesting the strong metal-support interaction between the PtFe intermetallic and the FeN_4CCl support. In addition, the fitting results of the EXAFS curve also reveal that the coordination number is approximately 6.25 for the Pt–Pt shell, approximately 4.14 for the Pt–Fe shell and approximately 1.46 for the Pt–N shell. The optimized coordination environment and compressive strains described above enhance the catalytic activity of the ORR (Fig. S2 and

© 2024 The Author(s). Published by the Royal Society of Chemistry

Open Access Article. Published on 08 July 2024. Downloaded on 4/2/2026 6:00:46 PM.
This article is licensed under a Creative Commons Attribution-NonCommercial 3.0 Unported Licence.

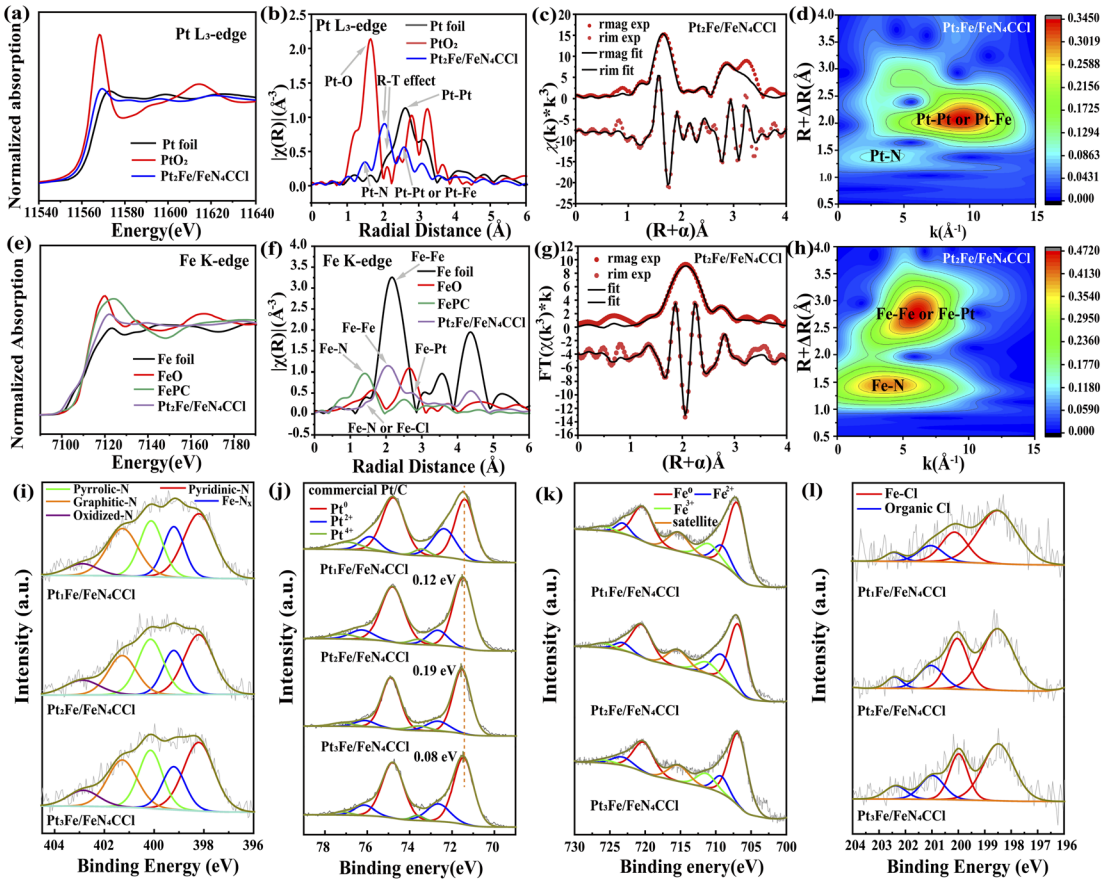

Fig. 2 (a–c) XAFS diagram of Pt L_3-edge XANES for Pt foil, PtO_2 and Pt_2Fe/FeN_4CCl (a), the Fourier transforms of EXAFS spectra for Pt foil, PtO_2 and Pt_2Fe/FeN_4CCl (b), the EXAFS fitting curve Pt L_3-edge of Pt_2Fe/FeN_4CCl catalyst at *R*-space (c) and wavelet transform of the Pt L_3-edge of corresponding EXAFS spectra for Pt_2Fe/FeN_4CCl catalyst (d). (e–h) XAFS diagram of Fe K-edge XANES for Fe foil, FeO, FePc and Pt_2Fe/FeN_4CCl (e), the Fourier transforms of EXAFS spectra for Fe foil, FeO, FePc and Pt_2Fe/FeN_4CCl (f), the EXAFS fitting curve Fe K-edge of Pt_2Fe/FeN_4CCl catalyst at *R*-space (g) and wavelet transform of the Fe K-edge of corresponding EXAFS spectra for Pt_2Fe/FeN_4CCl catalyst (h). (i–l) XPS spectra of N 1s (i), Pt 4f (j), Fe 2p (k) and Cl 2p (l).

Table S3†). Wavelet transform EXAFS spectroscopy could afford resolution in both radial distance and *k*-space. Incidentally, the scattering peak at ~2.05 Å is more likely assigned to the Ramsauer–Townsend effect, which is caused by the quantum effect rather than the superposition of the sine function because of the existence of heavy-metal elements. The Pt L_3-edge WT contour plots in the Pt_2Fe/FeN_4CCl catalyst show that the intensity maximum color with Pt–Pt/Pt–Fe bonds at ~9.5 $Å^{-1}$ is shifted upwards compared to Pt foil and PtO_2 (Fig. 2d and S3†).[32,33] Meanwhile, the XANES characterizations of the Pt_2Fe/FeN_4CCl catalyst and Fe foil, FeO, and phthalocyanine (FePc) are shown in Fig. 2e. The white line intensity of the Fe K-edge in Pt_2Fe/FeN_4CCl (~7122 eV) is located among those of Fe foil and FePc, indicating that the chemical state of Fe species in the Pt_2Fe/FeN_4CCl samples is probably concentrated on the metal Fe and oxidated Fe. Moreover, FT-EXAFS at the Fe K-edge presents primary peaks at ~1.5 Å, ~2.09 Å and ~2.72 Å, which are reasonably in line with the scattering paths of Fe–N/Fe–Cl,[34,35] Fe–Fe,[36] and Fe–Pt,[37] respectively (Fig. 2f). It is worth noting that the scattering paths Fe–N at ~1.5 Å probably offer evidence for the existence of the square-planar $Fe–N_4$ configuration with a porphyrin-like structure.[38,39] As a verification, the coordination configuration of the Fe atoms was analyzed by quantitatively fitting the EXAFS spectra. As shown in Fig. 2g, the fitted structural parameters suggest that a Fe atom is coordinated with one axial Cl atom at ~2.06 Å and four N atoms at ~1.92 Å, individually (Fig. S4 and Table S4†), substantiating that the three-dimensional FeN_4CCl architecture was attained (Fig. S5†). The fitting scattering path information benchmarked against Fe foil, FeO and FePc is plotted in Fig. S6.† The Fe K-edge WT contour plots of the Pt_2Fe/FeN_4CCl catalyst signify that the intensity maximum is ~4 $Å^{-1}$ for Fe–N/Fe–Cl and ~6.1 $Å^{-1}$ for FeFe/Fe–Pt and similar to the wavelet-transform contour plots of Fe foil, FeO and FePc, respectively (Fig. 2h and S7†).[40,41] These combined results further confirm the successful construction of FeN_4CCl moieties, the optimized axial-coordinated effect and the suitable electronic interface for intermediate adsorption and desorption.

X-ray photoelectron spectroscopy (XPS) further examined the surface chemical composition and electronic valence state of the as-prepared catalyst. The presence of Pt, Fe, Cl, N, C, and O elements was confirmed by the XPS survey of the Pt_xFe/FeN_4CCl

© 2024 The Author(s). Published by the Royal Society of Chemistry

Open Access Article. Published on 08 July 2024. Downloaded on 4/2/2026 6:00:46 PM. This article is licensed under a Creative Commons Attribution-NonCommercial 3.0 Unported Licence.

sample (Fig. S8 and Table S5†), which is consistent with the EDS profiles. The fitted peak of C 1s contains C–N peaks in contrast with the commercial Pt/C catalyst, indicating presumable nitrogen-doping in the as-prepared catalyst support (Fig. S9 and Table S6†). Notably, the fitted peaks of the characteristic N 1s spectra contain Fe–N_x peaks, further identifying the occurrence of FeN_4 sites, which matched with the XAFS analysis results (Fig. 2i and Table S7†).[42] Based on the peak fitting of Pt 4f (Fig. 2j, S10a and Table S8†), the Pt (0) mainly concentrates on the chemical state of the metal in commercial Pt/C, Pt_1Fe/FeN_4CCl, Pt_2Fe/FeN_4CCl, Pt_2Fe/FeN_4CCl and ordered PtFe NP catalysts, benefiting the acceleration of the entire ORR cycle.[43] Importantly, compared with the standard Pt 4f of Pt/C, the electron density of Pt (positive shift +0.12 eV for Pt_1Fe/FeN_4CCl, +0.19 eV for Pt_2Fe/FeN_4CCl and +0.08 eV for Pt_3Fe/FeN_4CCl, and negative shift −0.11 eV for ordered PtFe NPs, respectively) indicates the strong interactions between PtFe and FeN_4CCl.[44] However, the Pt_2Fe/FeN_4CCl catalyst was modified with the FeN_4CCl support, which drew plenty of electrons due to the strong electronegativity of the Cl ligands (3.16), thus resulting in a positive binding energy shift. Furthermore, a negative binding energy shift was exhibited for Fe 2p on Pt_2Fe/FeN_4CCl (−0.26 eV) as compared to the FeN_4C SACs at 707.03 eV, demonstrating that the axial-coordinated traction effect of the Cl ligands regulates the electron structure (Fig. 2k, S10b and Table S9†). Meanwhile, the Fe 2p of ordered PtFe NPs (0.14 eV) suggests a positive binding energy shift compared with Pt_2Fe/FeN_4CCl at 706.77 eV, in line with the Pt 4f results. Combined with the Cl 2p characteristic spectrum, the Cl species mainly exist in the form of Fe–Cl coordination (Fig. 2l and Table S10†), suggesting that the Cl atoms are axial-coordinated with the FeN_4 site, benefiting the adsorption/desorption conversion process.

2.2 ORR performance of the Pt_xFe/FeN_4CCl system

The primary ORR activity of the FeN_4C SACs, Pt_1Fe/FeN_4CCl, Pt_2Fe/FeN_4CCl, Pt_3Fe/FeN_4CCl, ordered PtFe NPs and commercial Pt/C catalysts was investigated by cyclic voltammetry (CV) and linear sweep voltammetry (LSV) in N_2 and O_2 saturated $HClO_4$ solutions, respectively. As shown in Fig. S11a and b†, the CV curves show that the hydrogen adsorption/desorption peaks appear in the region of 0–0.4 V and the Pt oxidation/reduction peaks appear at 0.6–1.2 V, respectively. Moreover, as shown in Fig. 3a and S11c,† the Pt_2Fe/FeN_4CCl shows a higher ORR activity with a half-wave potential ($E_{1/2}$) of 0.936 V *vs.* reversible hydrogen electrode (RHE) relative to the FeN_4C SACs (0.851 V), Pt_1Fe/FeN_4CCl (0.909 V), Pt_3Fe/FeN_4CCl (0.920 V), ordered PtFe NPs (0.903 V) and commercial Pt/C (0.876 V) catalysts. The Tafel slope as a significant kinetic parameter is displayed in Fig. 3b and S11d.† The value of the Tafel slope for the Pt_2Fe/FeN_4CCl (57.75 mV dec^{-1}) sample is lower than that of the FeN_4C SACs (117.24 mV dec^{-1}), Pt_1Fe/FeN_4CCl (65.11 mV dec^{-1}), Pt_3Fe/FeN_4CCl (70.53 mV dec^{-1}), ordered PtFe NPs (72.35.35 mV dec^{-1}) and commercial Pt/C (77.59 mV dec^{-1}) counterparts, indicating the higher ORR kinetics of the Pt_2Fe/FeN_4CCl one. The electrochemical surface area (ECSA) was measured to further evaluate the ORR intrinsic activity by CO-stripping experiments, instead of hydrogen underpotential deposition (HUPD), considering the suppression of H_{upd} adsorption on Pt–M alloy catalysts.[45] The mass activity (MA) and specific activity (SA) at 0.9 V *vs.* RHE of all the catalysts were calculated by normalizing the Pt loading and ECSA (Table S11†). As shown in Fig. 3c, d and S11e,† the MA/SA of Pt_2Fe/FeN_4CCl was 1.637 A mg_{Pt}^{-1}/2.270 mA cm^{-2}, which is about 2.71/2.53, 2.22/2.14, 3.13/2.66 and 9.92/8.60 times higher than that of Pt_1Fe/FeN_4CCl (0.605 A mg_{Pt}^{-1}/0.899 mA cm^{-2}), Pt_3Fe/FeN_4CCl (0.738 A mg_{Pt}^{-1}/1.061 mA cm^{-2}), ordered PtFe NPs (0.523 A mg_{Pt}^{-1}/0.852 mA cm^{-2}) and commercial Pt/C (0.165 A mg_{Pt}^{-1}/0.264 mA cm^{-2}), respectively. For the FeN_4C SACs, the ORR activity was further evaluated by the half-wave potential and the kinetic current density (j_k), indicating that all of the as-prepared Pt-based catalysts exhibited superior ORR performance (Fig. S11f†). In addition, Fig. 3e and S12† show that the average electron transfer number (n) was calculated as 3.89 for Pt_2Fe/FeN_4CCl, 3.85 for Pt_1Fe/FeN_4CCl, 3.83 for Pt_3Fe/FeN_4CCl and 3.71 for commercial Pt/C by the Koutecky–Levich (K–L) equation, demonstrating the unabridged four-electron ($4e^-$) ORR pathway with the reduction of O_2 to H_2O directly.[46] The stability of the as-prepared catalysts and commercial Pt/C for the ORR was investigated *via* an accelerated durability test (ADT) in O_2 saturated 0.1 M $HClO_4$ solution. Fig. S13† displays a larger negative shift (49 mV) of $E_{1/2}$ for commercial Pt/C before and after 30 000 potential cycles. Further, the calculated MA and SA of commercial Pt/C seriously decreased by 38.25% and 57.94% relative to the original values, respectively. In contrast, the as-prepared Pt_xFe/FeN_4CCl catalyst exhibited enhanced ORR performance (Table S12†). The Pt_2Fe/FeN_4CCl sample acquired more favourable retention of catalytic activity (only 16 mV negative shift of $E_{1/2}$) after 40 000 sweeping cycles (Fig. 3f) and afforded a slight loss of 7.80% in MA and 8.82% in SA (Fig. 3g and h). Meanwhile, the LSV curves of the as-prepared Pt_1Fe/FeN_4CCl and the Pt_3Fe/FeN_4CCl catalyst exhibit 21 mV and 24 mV negative shift of $E_{1/2}$ before and after 40 000 cycles (Fig. S14†), along with exiguous drops of 12.50% and 17.61% for Pt_1Fe/FeN_4CCl as well as 15.41% and 19.30% for Pt_3Fe/FeN_4CCl in MA and SA, respectively. Moreover, the ORR performance of the as-prepared Pt_2Fe/FeN_4CCl catalyst with optimum surface composition is superior to the reported literature (Table S13†).

To further verify the morphology after ADT, CO stripping experiments of Pt_1Fe/FeN_4CCl, Pt_2Fe/FeN_4CCl, Pt_3Fe/FeN_4CCl and commercial Pt/C are shown in Fig. 3i and S15.† The onset potential of the CO oxidation peak of all as-prepared catalysts is much lower than that of commercial Pt/C and fractionally deviated before and after 40 000 CV cycles, indicating the maintenance of the electronic structure and surface composition.[47] Such results demonstrate that the enhanced ORR activity and stability of the as-prepared Pt_xFe/FeN_4CCl catalyst was attributed to the construction of an FeN_4CCl moiety with optimized orbital electron-delocalization, the formation of an ordered phase with a definite atomic distribution and surface composition, and strong interaction between the PtFe intermetallic and FeN_4CCl substrate.

Open Access Article. Published on 08 July 2024. Downloaded on 4/2/2026 6:00:46 PM.
This article is licensed under a Creative Commons Attribution-NonCommercial 3.0 Unported Licence.

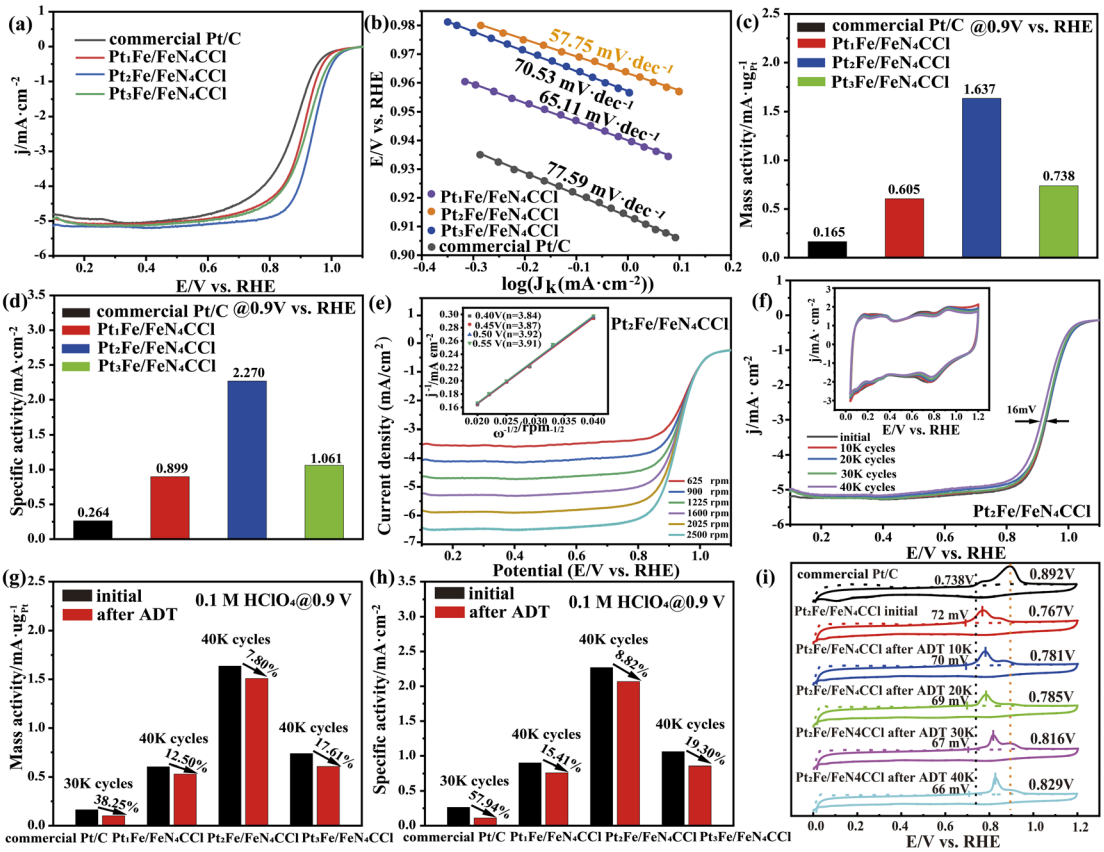

Fig. 3 (a) LSV curves of Pt_1Fe/FeN_4CCl, Pt_2Fe/FeN_4CCl, Pt_3Fe/FeN_4CCl, and commercial Pt/C catalysts in O_2-saturated 0.1 M $HClO_4$ solution, with sweep rate 10 mV s^{-1}, and rotation rate 1600 rpm. (b) Tafel plots of Pt_1Fe/FeN_4CCl, Pt_2Fe/FeN_4CCl, Pt_3Fe/FeN_4CCl, and commercial Pt/C catalysts. (c and d) MA and SA of Pt_1Fe/FeN_4CCl, Pt_2Fe/FeN_4CCl, Pt_3Fe/FeN_4CCl, and commercial Pt/C catalysts. (e) ORR polarization curves of Pt_2Fe/FeN_4CCl catalysts at various rotation rates and Koutecky–Levich plots at various electrode potentials. (f) ORR polarization curves of the Pt_2Fe/FeN_4CCl catalysts before and after 40 000 sweeping cycles (the inset shows the CV curves of Pt_2Fe/FeN_4CCl). (g and h) The changes of MA and SA of Pt_1Fe/FeN_4CCl, Pt_2Fe/FeN_4CCl, Pt_3Fe/FeN_4CCl, and commercial Pt/C catalysts before and after ADT in different cycles. (i) CO stripping voltammetry in 0.1 M $HClO_4$ electrolyte of the Pt_2Fe/FeN_4CCl catalyst compared with commercial Pt/C.

2.3 Density functional theory computational analysis

Density functional theory (DFT) was carried out to clarify the influence of the PtFe/FeN_4CCl structure on the ORR catalytic process. The constructed structural models (after optimization) of FeN_4C, FeN_4CCl, PtFe and PtFe/FeN_4CCl, based on the.

AC-HAADF-TEM images, XAFS and the corresponding fitting results, and XPS signal analysis, are shown in Fig. S16.† Fig. 4a and S17† exhibit the two-dimensional electron localization function (2D ELF) of the FeN_4 part in FeN_4C, FeN_4CCl and PtFe/FeN_4CCl, as well as the PtFe part in PtFe/FeN_4CCl, in which the FeN_4 part possesses a symmetrical electron localization distribution. The bright region on the Fe site of FeN_4CCl and PtFe/FeN_4CCl becomes darker compared to FeN_4C, testifying that the orbital electron delocalization effect exists induced by the axial-coordinated traction of Cl atoms.[48,49] In comparison, the overall color of Pt atoms is brighter compared to the Fe atoms in the PtFe part, which is caused by the significant charge polarization by the electron delocalization degree of both Pt and Fe atoms with different electronegativity.[50] A similar conclusion is drawn from the differential spin density distribution (Fig. S18†). Fig. 4b displays the charge density difference (CDD) of FeN_4C, FeN_4CCl, FeN_4CCl–PtFe, and PtFe–FeN_4CCl, in which the metal site evidently confirms an inclination to bereft electrons. There appear extremely palpable charge separation/transfer effects around the PtFe intermetallic and the FeN_4CCl substrate, exemplifying its interaction with the supports and accordingly benefiting the first adsorption of O_2 in conjunction with the following four-electron step process. More precisely, compared with FeN_4C and Fe_4CCl, the FeN_4CCl substrate in the PtFe/FeN_4CCl catalyst can absorb a significant number of electrons from the PtFe intermetallic and form a remarkable positive charge area due to the occurrence of the axial-coordinated Cl atoms. Previous research studies have manifested that electron deficient (or positively charged) metal sites are instrumental in attenuating the adsorption free energy of OH_{abs} intermediates.[51] Bader charge quantifiable analysis in Fig. 4c and S19† further confirms this viewpoint. When a Cl atom axially coordinated the modified FeN_4 site, the Fe center electron transfer of both PtFe/FeN_4CCl (1.18|e|) and FeN_4CCl (1.16|e|) is clearly more than in FeN_4C (1.11|e|). Consistently, while the ordered PtFe nanoparticles embedded into the atomically dispersed chlorine-nitrogen-doped Fe single-atom support, the Pt center in the

© 2024 The Author(s). Published by the Royal Society of Chemistry

Open Access Article. Published on 08 July 2024. Downloaded on 4/2/2026 6:00:46 PM.
This article is licensed under a Creative Commons Attribution-NonCommercial 3.0 Unported Licence.

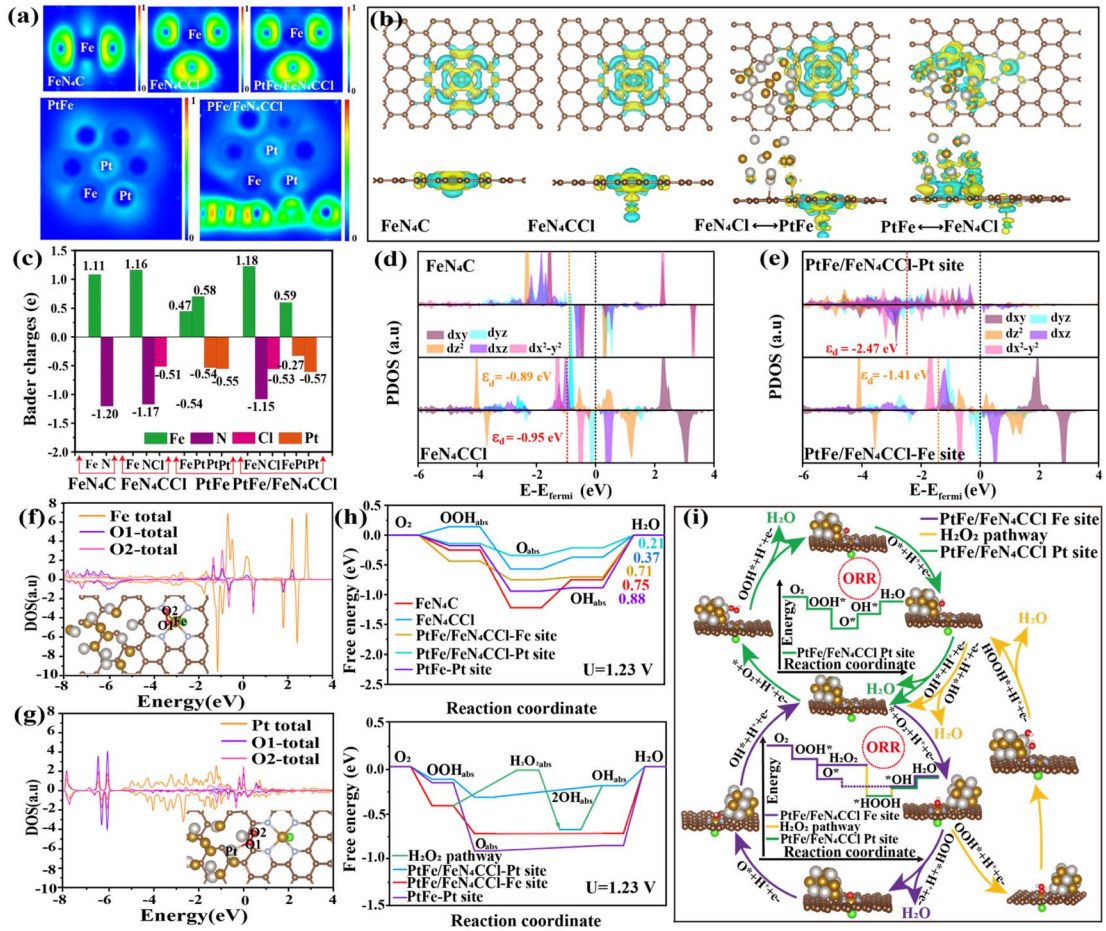

Fig. 4 (a) ELF of the center Fe site (the top shows FeN_4C, FeN_4CCl, and $PtFe/FeN_4CCl$) and the center Pt site (the bottom shows PtFe and PtFe/FeN_4CCl). Scale bars, 0–1. (b) Top and side views of the 3D charge density differences for FeN_4C, FeN_4CCl, FeN_4CCl ↔ PtFe and PtF ↔ eFeN_4CCl, respectively. (c) The value of transferred Bader charges of FeN_4C, FeN_4CCl, PtFe, and $PtFe/FeN_4CCl$ at the metal site (Fe and Pt) and the surrounding atoms in the corresponding structural models. (d) PDOS of Fe-3d in FeN_4C and FeN_4CCl. (e) PDOS of the Fe and Pt sites in PtFe/FeN_4CCl. (f and g) After the $PtFe/FeN_4CCl$ system interacts with O_2, the DOS diagram of the adsorption metal site (Fe and Pt) with O1 and O2, respectively. (h) (top) Free energy diagrams of different ORR intermediates at 1.23 V and (bottom) ORR catalytic process involved in the H_2O_2 intermediate over the $PtFe/FeN_4CCl$–Pt site and PtFe–Pt site as well as the $PtFe/FeN_4CCl$–Fe site, FeN_4C, and FeN_4CCl. (i) Scheme of the pathway in the ORR cycle of $PtFe/FeN_4CCl$ based on DFT.

$PtFe/FeN_4CCl$ catalyst showed charge accumulation less than that of PtFe without a modified Cl atom. These numerical results attest that the axial-coordinated Cl atoms can regulate the electronic structure of the active site, in line with the observation of the above CDD data.[52,53] The effect of axial-coordinated Cl atoms on the electron distribution was further investigated by partial density of states (PDOS) calculations. As shown in Fig. 4d, e and S20,† the d-band center of Fe-3d in FeN_4CCl and $PtFe/FeN_4CCl$ (−0.95 eV and −1.41 eV) shifts down in comparison to FeN_4C (−0.89 eV). The $PtFe/FeN_4CCl$ (−2.47 eV) exhibits a downshifted d-band center compared with PtFe (−2.33 eV). It is evidently demonstrated that the axial-coordinated Cl atoms arouse Fe center electron transfer, inducing the occupancy of orbital electron delocalization,[54,55] which is consistent with the calculated magnetic moment (Table S14†) and spin density distribution.

To further verify the synergistic ORR catalysis mechanism, we calculated the density of states (DOS) of the active site and O_2 molecule to perceive the activation mechanism of $O_{2,abs}$. According to molecular orbital theory, the DOS of both O1 and O2 atoms in the O_2 molecule is entirely symmetric (Fig. S21†).[56] When an O_2 molecule adsorbed on the Fe sites in $PtFe/FeN_4CCl$ (Fig. 4f, S22a and b†), FeN_4C (Fig. S23a–c†), and FeN_4CCl (Fig. S23d–f†), the DOS shows significantly discrete Fe 3d and O 2p orbital states. In contrast, when an O_2 molecule adsorbs on the Pt sites in both $PtFe/FeN_4CCl$ (Fig. 4g, S22c and d†) and PtFe (Fig. S23g–i†), the DOS shows a symmetric arrangement in the spin channels (spin-up and spin-down). Meanwhile, the O 2p orbital splits into discrete levels and the intensity of the localized Pt 3d states is significantly reduced, suggesting that the O_2 molecules are better activated.[57] Utilizing the free energy step diagram, the potential-determining-step (PDS) from OH_{abs} to H_2O in the ORR transversion on $PtFe/FeN_4CCl$ is more likely to occur than in FeN_4C, FeN_4CCl and PtFe (Fig. 4h and S24†). When the voltage is 1.23 V, the PDS of the $PtFe/FeN_4CCl$–Pt site is the desorption of OH_{abs} ($OH_{abs} + H^+ + e^- \rightarrow H_2O_{abs}$).

Open Access Article. Published on 08 July 2024. Downloaded on 4/2/2026 6:00:46 PM.
This article is licensed under a Creative Commons Attribution-NonCommercial 3.0 Unported Licence.

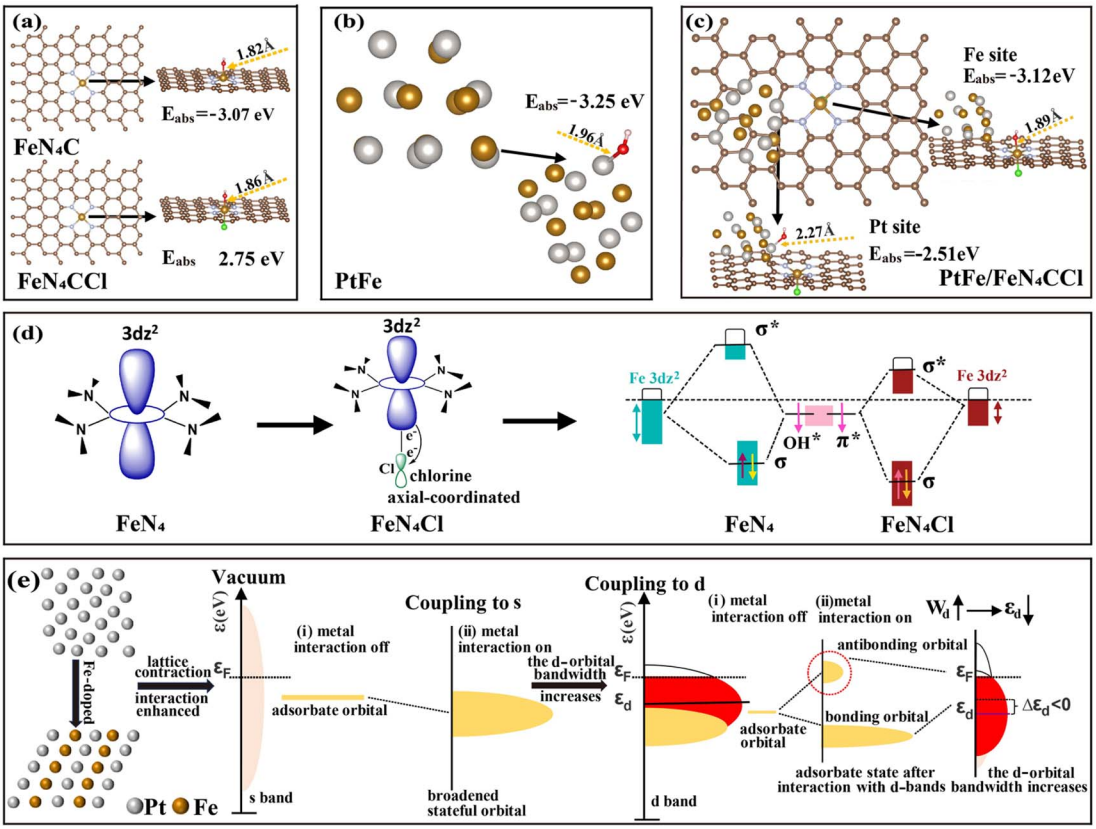

Fig. 5 (a–c) The bond lengths and corresponding adsorption free energy with an oxygen intermediate on active sites (Fe and Pt). (d) The axial-coordinated Cl atoms lead to an orbital electron delocalization effect of the Fe 3d orbitals. (e) The schematic diagram of alloying Pt with a non-precious Fe element, which can exhibit a lattice contraction compared with pure Pt. The alteration of the d-band center could affect its absorption capability of oxygen-containing intermediates.

Obviously, the PtFe/FeN_4CCl–Pt site has a smaller Gibbs free energy change (ΔG_{pds}) (0.21 eV) relative to the FeN_4C (0.75 eV), FeN_4CCl (0.37 eV), PtFe (0.88 eV), and PtFe/FeN_4CCl–Fe site (0.71 eV), indicating that the synergistic effect of the PtFe intermetallic and FeN_4CCl support enhances the catalytic efficiency and accelerates the ORR cycle. In addition, DFT calculations were carried out to clarify the potential determining step (PDS) of the free energy step diagram for the ORR catalytic process based on electrochemical tests.[58] The DFT calculation results showed that the HOOH intermediates at Fe sites can release and migrate to the contiguous Pt sites for successive reactions, thereby effectuating integral oxygen reduction (Fig. 4i and S25†).[59,60] Such a result proved that the synergistic effect between the PtFe intermetallic and FeN_4CCl sites in the ORR process actualizes the four-electron transfer pathway.

To trace back the reason for the higher activity of PtFe/FeN_4CCl, the interaction between the catalytic site and OH_{abs} intermediate species was investigated. The bond length of Fe–OH in optimized models of the FeN_4C, FeN_4CCl, and PtFe/FeN_4CCl–Fe sites is $L_{Fe-OH} = 1.82$ Å, $L_{Fe-OH} = 1.86$ Å, and $L_{Fe-OH} = 1.89$ Å, individually. Identically, the bond length of Pt–OH of the PtFe and PtFe/FeN_4CCl–Pt site is $L_{Pt-OH} = 1.96$ Å and $L_{Pt-OH} = 2.27$ Å, respectively, which reveals that activation of the O_2 molecule is easier to implement on the PtFe/FeN_4CCl–Pt active sites (Fig. 5a–c). Synchronously, the adsorption free energy (E_{abs}) of OH_{abs} species on the Fe sites of FeN_4C, Fe sites of FeN_4CCl, Fe sites of PtFe/FeN_4CCl–Fe, Pt sites of PtFe, and Pt sites of PtFe/FeN_4CCl–Pt are $E_{abs} = -3.07$ eV, $E_{abs} = -2.75$ eV, $E_{abs} = -3.12$ eV, $E_{abs} = -3.25$ eV, and $E_{abs} = -2.51$ eV, respectively. Due to the axial-coordinated Cl atoms pulling more electrons to deviate from the central metal atoms, the electronic circumstances were directly revised by orbital electron delocalization, which weakens the binding strength between the catalyst surface and the adsorbates. As shown in Fig. 5d, the interaction between the Fe $3d_{z^2}$ orbitals and Cl $3p_z$ orbitals contributes to strong d_{z^2}–p_z hybridization. The electron delocalization between the $3d_{z^2}$ orbital in the FeN_4 moiety and the 2p orbitals of the oxygen intermediates could tune the energy levels, splitting into bonding orbitals and antibonding states. The d_{z^2}-state energy level of the active site modified with axial-coordinated Cl atoms commonly down-shifts from the Fermi level.[61] Additionally, according to d-band theory, the alteration of the d-band center could affect its absorption capability of oxygen-containing intermediates.[62,63] Pt is alloyed with a non-precious Fe element, which can exhibit a lattice contraction and a surface strain effect compared with pure Pt (Fig. 5c). When oxygen-containing intermediates hybridize with a broader d band, the adsorbate state splits into a localized

© 2024 The Author(s). Published by the Royal Society of Chemistry

Open Access Article. Published on 08 July 2024. Downloaded on 4/2/2026 6:00:46 PM. This article is licensed under a Creative Commons Attribution-NonCommercial 3.0 Unported Licence.

bonding orbital and antibonding orbital.[64] The more electron occupancies of the antibonding orbitals could downgrade the energy level of the d-band center, thereby weakening the active site adsorption energy. Besides, the PtFe intermetallic emanates the structurally ordered atomic arrangement and uniquely local geometrical properties, thus tremendously heightening higher ORR stability and activity.

3. Conclusions

In summary, a synergistic ORR catalyst with an orbital electron delocalization axial-coordinated effect was successfully synthesized by utilizing hemin as a precursor in high-temperature pyrolysis. The unique structure of the as-prepared catalyst, such as the ordered atomic arrangement and FeN_4CCl support with atomically dispersed Fe single-atoms, was confirmed by the AC-HAADF-STEM images. XAFS analysis further demonstrates the existence of the FeN_4Cl moiety with an Fe single-atom structure and the axial chlorine-coordinated coupling induction of the FeN_4CCl substrate by configuring the Fe–N bond for ~1.92 Å and Fe–Cl bond for ~2.06 Å. More importantly, ELF and DFT further determine an orbital electron delocalization effect between the Cl atoms and the FeN_4, resulting in electron redistribution and coordinated surroundings modification, thus optimizing the adsorption free energy of the OH_{abs} intermediates for accelerating the electrocatalytic kinetics. Specifically, the obtained Pt_2Fe/FeN_4CCl catalyst with optimum surface composition displayed a higher catalytic performance, which was 9.92 times in MA, and 8.60 times in SA relative to the commercial Pt/C catalyst, respectively. The LSV loss of $\Delta E_{1/2} = 16$ mV was observed after 40 000 cycles before and after ADT, along with affording a marginal loss of 7.80% in MA and 8.82% in SA at a potential of 0.9 V *vs.* RHE, respectively. The heightened catalytic performance can be attributed not only to the orbital electron delocalization of the axial-coordinated modified FeN_4CCl substrate, but also to the synergistic catalysis with the structurally ordered PtFe intermetallic. Our work manifests the crucial role of regulating the chemical environment of materials to optimize their electronic structure in catalysis and provides an alternative insight into designing synergistically efficient ORR catalysts.

4. Experimental section

Experimental procedures, material characterization, electrochemical measurements, and DFT computational details are provided in the Electronic ESI.†

Data availability

The authors declare that the data are available within the paper and its ESI† file.

Author contributions

Chenzhong Wu: conceptualization, investigation, writing – original draft. Meida Chen: data curation, methodology validation. Bin Wang: data curation, visualization. Leqing Luo: data curation. Qian Zhou: data curation. Guangtao Mao: resources, visualization. Yuan Xiong: resources, visualization. Qingmei Wang: supervision, writing – review & editing, funding acquisition.

Conflicts of interest

The authors declare no conflict of interest.

Acknowledgements

This research work was financially supported by the National Natural Science Foundation of China (No. 22169005, 22068009 and 22262006), the Science and Technology Support Project of Guizhou Provincial Science and Technology Department (No. ZK[2023]050 and [2023]403), and the Open Project of Institute of Dual-carbon and New Energy Technology Innovation and Development of Guizhou Province (No. DCRE-2023-06).

Notes and references

1 E. B. Tetteh, H.-Y. Lee, C.-H. Shin, S.-h. Kim, H. C. Ham, T.-N. Tran, J.-H. Jang, S. J. Yoo and J.-S. Yu, New PtMg Alloy with Durable Electrocatalytic Performance for Oxygen Reduction Reaction in Proton Exchange Membrane Fuel Cell, *ACS Energy Lett.*, 2020, **5**(5), 1601–1609.

2 F. Zhu, K. Xu, F. He, Y. Xu, Z. Du, H. Zhang, D. Zeng, Y. Liu, H. Wang, D. Ding, Y. Zhou and Y. Chen, An Active and Contaminants-Tolerant High-Entropy Electrode for Ceramic Fuel Cells, *ACS Energy Lett.*, 2024, **9**(2), 556–567.

3 X. Wei, S. Song, W. Cai, Y. Kang, Q. Fang, L. Ling, Y. Zhao, Z. Wu, X. Song, X. Xu, S. M. Osman, W. Song, T. Asahi, Y. Yamauchi and C. Zhu, Pt Nanoparticle–Mn Single-Atom Pairs for Enhanced Oxygen Reduction, *ACS Nano*, 2024, **18**(5), 4308–4319.

4 F. Xiao, Q. Wang, G.-L. Xu, X. Qin, I. Hwang, C.-J. Sun, M. Liu, W. Hua, H.-w. Wu, S. Zhu, J.-C. Li, J.-G. Wang, Y. Zhu, D. Wu, Z. Wei, M. Gu, K. Amine and M. Shao, Atomically dispersed Pt and Fe sites and Pt–Fe nanoparticles for durable proton exchange membrane fuel cells, *Nat. Catal.*, 2022, **5**(6), 503–512.

5 F. Chen, S. Chen, A. Wang, M. Wang, L. Guo and Z. Wei, Blocking the sulfonate group in Nafion to unlock platinum's activity in membrane electrode assemblies, *Nat. Catal.*, 2023, **6**(5), 392–401.

6 W. Li, B. Liu, D. Liu, P. Guo, J. Liu, R. Wang, Y. Guo, X. Tu, H. Pan, D. Sun, F. Fang and R. Wu, Alloying Co Species into Ordered and Interconnected Macroporous Carbon Polyhedra for Efficient Oxygen Reduction Reaction in Rechargeable Zinc–Air Batteries, *Adv. Mater.*, 2022, **34**(17), 2109605.

7 P. Xiong, H. Niu, Z. Zhu, L. Zhao, J. Zuo, S. Gong, X. Niu, J. Chen, R. Wu and B. Xia, Engineering a High-Loading Sub-4 nm Intermetallic Platinum–Cobalt Alloy on Atomically Dispersed Cobalt–Nitrogen–Carbon for Efficient

Open Access Article. Published on 08 July 2024. Downloaded on 4/2/2026 6:00:46 PM. This article is licensed under a Creative Commons Attribution-NonCommercial 3.0 Unported Licence.

Oxygen Reduction in Fuel Cells, *Nano Lett.*, 2024, **24**(13), 3961–3970.

8 K. Wang, H. Yang, Q. Wang, J. Yu, Y. He, Y. Wang, S. Song and Y. Wang, Electronic Enhancement Engineering by Atomic Fe–N_4 Sites for Highly-Efficient PEMFCs: Tailored Electric-Thermal Field on Pt Surface, *Adv. Energy Mater.*, 2023, **13**(14), 2204371.

9 M. Chen, Y. He, J. S. Spendelow and G. Wu, Atomically Dispersed Metal Catalysts for Oxygen Reduction, *ACS Energy Lett.*, 2019, **4**(7), 1619–1633.

10 H. Yang, Y. Liu, X. Liu, X. Wang, H. Tian, G. I. N. Waterhouse, P. E. Kruger, S. G. Telfer and S. Ma, Large-scale synthesis of N-doped carbon capsules supporting atomically dispersed iron for efficient oxygen reduction reaction electrocatalysis, *eScience*, 2022, **2**(2), 227–234.

11 S. Yin, Y.-N. Yan, L. Chen, N. Cheng, X. Cheng, R. Huang, H. Huang, B. Zhang, Y.-X. Jiang and S.-G. Sun, FeN_4 Active Sites Electronically Coupled with PtFe Alloys for Ultralow Pt Loading Hybrid Electrocatalysts in Proton Exchange Membrane Fuel Cells, *ACS Nano*, 2023, **18**(1), 551–559.

12 Z. Qiao, C. Wang, Y. Zeng, J. S. Spendelow and G. Wu, Advanced Nanocarbons for Enhanced Performance and Durability of Platinum Catalysts in Proton Exchange Membrane Fuel Cells, *Small*, 2021, **17**(48), 2006805.

13 H. Adabi, A. Shakouri, N. Ul Hassan, J. R. Varcoe, B. Zulevi, A. Serov, J. R. Regalbuto and W. E. Mustain, High-performing commercial Fe–N–C cathode electrocatalyst for anion-exchange membrane fuel cells, *Nat. Energy*, 2021, **6**(8), 834–843.

14 M. Liu, T. Sun, T. Peng, J. Wu, J. Li, S. Chen, L. Zhang, S. Li, J. Zhang and S. Sun, Fe-NC Single-Atom Catalyst with Hierarchical Porous Structure and P–O Bond Coordination for Oxygen Reduction, *ACS Energy Lett.*, 2023, **8**(11), 4531–4539.

15 C. H. Choi, H.-K. Lim, M. W. Chung, G. Chon, N. Ranjbar Sahraie, A. Altin, M.-T. Sougrati, L. Stievano, H. S. Oh, E. S. Park, F. Luo, P. Strasser, G. Dražić, K. J. J. Mayrhofer, H. Kim and F. Jaouen, The Achilles' heel of iron-based catalysts during oxygen reduction in an acidic medium, *Energy Environ. Sci.*, 2018, **11**(11), 3176–3182.

16 Y. Wang, X. Huang and Z. Wei, Recent developments in the use of single-atom catalysts for water splitting, *Chin. J. Catal.*, 2021, **42**(8), 1269–1286.

17 Z.-y. Mei, S. Cai, G. Zhao, Q. Jing, X. Sheng, J. Jiang and H. Guo, Understanding electronic configurarions and coordination environment for enhanced ORR process and improved Zn-air battery performance, *Energy Storage Mater.*, 2022, **50**, 12–20.

18 J. Yu, C. Su, L. Shang and T. Zhang, Single-Atom-Based Oxygen Reduction Reaction Catalysts for Proton Exchange Membrane Fuel Cells: Progress and Perspective, *ACS Nano*, 2023, **17**(20), 19514–19525.

19 H. Chen, C. He, H. Niu, c. Xia, F. Li, W. Zhao, F. Song, T. Yao, Y. Chen, Y. Su, W. Guo and B. Xia, Surface Redox Chemistry Regulates the Reaction Microenvironment for Efficient Hydrogen Peroxide Generation, *J. Am. Chem. Soc.*, 2024, **146**(22), 15356–15365.

20 W.-J. Zeng, C. Wang, Q.-Q. Yan, P. Yin, L. Tong and H.-W. Liang, Phase diagrams guide synthesis of highly ordered intermetallic electrocatalysts: separating alloying and ordering stages, *Nat. Commun.*, 2022, **13**(1), 7654.

21 J. Guan, S. Yang, T. Liu, Y. Yu, J. Niu, Z. Zhang and F. Wang, Intermetallic FePt@PtBi Core–Shell Nanoparticles for Oxygen Reduction Electrocatalysis, *Angew. Chem., Int. Ed.*, 2021, **60**(40), 21899–21904.

22 Y. Shi, W. Yang, W. Gong, X. Wang, Y. Zhou, X. Shen, Y. Wu, J. Di, D. Zhang and Q. Li, Interconnected surface-vacancy-rich PtFe nanowires for efficient oxygen reduction, *J. Mater. Chem. A*, 2021, **9**(21), 12845–12852.

23 X. Zou, S. Chen, Q. Wang, X. Gao, J. Li, J. Li, L. Li, W. Ding and Z. Wei, Leaching- and sintering-resistant hollow or structurally ordered intermetallic PtFe alloy catalysts for oxygen reduction reactions, *Nanoscale*, 2019, **11**(42), 20115–20122.

24 M. Chen, S. Zhou, W. Liao, Z. Wang, J. Long, Q. Zhou and Q. Wang, Ordered PtCo Intermetallics Featuring Nitrogen-Doped Carbon Prepared by Surface Coating Strategy for Oxygen Reduction Reaction, *Chemelectrochem*, 2022, **9**(20), e202200803.

25 Q. Wang, H. Tang, M. Wang, L. Guo, S. Chen and Z. Wei, Precisely tuning the electronic structure of a structurally ordered PtCoFe alloy *via* a dual-component promoter strategy for oxygen reduction, *Chem. Commun.*, 2021, **57**(33), 4047–4050.

26 T. Y. Yoo, J. Lee, S. Kim, M. Her, S.-Y. Kim, Y.-H. Lee, H. Shin, H. Jeong, A. K. Sinha, S.-P. Cho, Y.-E. Sung and T. Hyeon, Scalable production of an intermetallic Pt–Co electrocatalyst for high-power proton-exchange-membrane fuel cells, *Energy Environ. Sci.*, 2023, **16**(3), 1146–1154.

27 B. Liu, R. Feng, M. Busch, S. Wang, H. Wu, P. Liu, J. Gu, A. Bahadoran, D. Matsumura, T. Tsuji, D. Zhang, F. Song and Q. Liu, Synergistic Hybrid Electrocatalysts of Platinum Alloy and Single-Atom Platinum for an Efficient and Durable Oxygen Reduction Reaction, *ACS Nano*, 2022, **16**(9), 14121–14133.

28 Q. Cheng, S. Yang, C. Fu, L. Zou, Z. Zou, Z. Jiang, J. Zhang and H. Yang, High-loaded sub-6 nm Pt_1Co_1 intermetallic compounds with highly efficient performance expression in PEMFCs, *Energy Environ. Sci.*, 2022, **15**(1), 278–286.

29 J. Yang, R. Hübner, J. Zhang, H. Wan, Y. Zheng, H. Wang, H. Qi, L. He, Y. Li, A. A. Dubale, Y. Sun, Y. Liu, D. Peng, Y. Meng, Z. Zheng, J. Rossmeisl and W. Liu, A Robust PtNi Nanoframe/N-Doped Graphene Aerogel Electrocatalyst with Both High Activity and Stability, *Angew. Chem., Int. Ed.*, 2021, **60**(17), 9590–9597.

30 X. Zhao, H. Cheng, L. Song, L. Han, R. Zhang, G. Kwon, L. Ma, S. N. Ehrlich, A. I. Frenkel, J. Yang, K. Sasaki and H. L. Xin, Rhombohedral Ordered Intermetallic Nanocatalyst Boosts the Oxygen Reduction Reaction, *ACS Catal.*, 2020, **11**(1), 184–192.

31 N. Wang, R. Mei, X. Lin, L. Chen, T. Yang, Q. Liu and Z. Chen, Cascade Anchoring Strategy for Fabricating High-

 © 2024 The Author(s). Published by the Royal Society of Chemistry

Open Access Article. Published on 08 July 2024. Downloaded on 4/2/2026 6:00:46 PM. This article is licensed under a Creative Commons Attribution-NonCommercial 3.0 Unported Licence.

Loading Pt Single Atoms as Bifunctional Catalysts for Electrocatalytic Hydrogen Evolution and Oxygen Reduction Reactions, *ACS Appl. Mater. Interfaces*, 2023, **15**(24), 29195–29203.

32 J. Li, Q. Zhou, M. Yue, S. Chen, J. Deng, X. Ping, Y. Li, J. Li, Q. Liao, M. Shao and Z. Wei, Cross-linked multi-atom Pt catalyst for highly efficient oxygen reduction catalysis, *Appl. Catal. B Environ.*, 2021, **284**, 119728.

33 X. Wang, N. Fu, J.-C. Liu, K. Yu, Z. Li, Z. Xu, X. Liang, P. Zhu, C. Ye, A. Zhou, A. Li, L. Zheng, L.-M. Liu, C. Chen, D. Wang, Q. Peng and Y. Li, Atomic Replacement of PtNi Nanoalloys within Zn-ZIF-8 for the Fabrication of a Multisite CO_2 Reduction Electrocatalyst, *J. Am. Chem. Soc.*, 2022, **144**(50), 23223–23229.

34 W. Chen, W. Gao, P. Tu, T. Robert, Y. Ma, H. Shan, X. Gu, W. Shang, P. Tao, C. Song, T. Deng, H. Zhu, X. Pan, H. Yang and J. Wu, Neighboring Pt Atom Sites in an Ultrathin FePt Nanosheet for the Efficient and Highly CO-Tolerant Oxygen Reduction Reaction, *Nano Lett.*, 2018, **18**(9), 5905–5912.

35 S. Ding, J. A. Barr, Q. Shi, Y. Zeng, P. Tieu, Z. Lyu, L. Fang, T. Li, X. Pan, S. P. Beckman, D. Du, H. Lin, J.-C. Li, G. Wu and Y. Lin, Engineering Atomic Single Metal–FeN_4Cl Sites with Enhanced Oxygen-Reduction Activity for High-Performance Proton Exchange Membrane Fuel Cells, *ACS Nano*, 2022, **16**(9), 15165–15174.

36 X. Ao, W. Zhang, B. Zhao, Y. Ding, G. Nam, L. Soule, A. Abdelhafiz, C. Wang and M. Liu, Atomically dispersed Fe–N–C decorated with Pt-alloy core–shell nanoparticles for improved activity and durability towards oxygen reduction, *Energy Environ. Sci.*, 2020, **13**(9), 3032–3040.

37 M. Jiang, W. Liu, X. Yang, Z. Jiang, T. Yao, S. Wei and X. Peng, Pt/Fe_3O_4 Core/Shell Triangular Nanoprisms by Heteroepitaxy: Facet Selectivity at the Pt–Fe_3O_4 Interface and the Fe_3O_4 Outer Surface, *ACS Nano*, 2015, **9**(11), 10950–10960.

38 Y. Chen, Z. Li, Y. Zhu, D. Sun, X. Liu, L. Xu and Y. Tang, Atomic Fe Dispersed on N-Doped Carbon Hollow Nanospheres for High-Efficiency Electrocatalytic Oxygen Reduction, *Adv. Mater.*, 2018, **31**(8), 1806312.

39 X. Wan, X. Liu, Y. Li, R. Yu, L. Zheng, W. Yan, H. Wang, M. Xu and J. Shui, Fe–N–C electrocatalyst with dense active sites and efficient mass transport for high-performance proton exchange membrane fuel cells, *Nat. Catal.*, 2019, **2**(3), 259–268.

40 F. Xiao, G.-L. Xu, C.-J. Sun, I. Hwang, M. Xu, H.-w. Wu, Z. Wei, X. Pan, K. Amine and M. Shao, Durable hybrid electrocatalysts for proton exchange membrane fuel cells, *Nano Energy*, 2020, **77**, 105192.

41 A. Zitolo, V. Goellner, V. Armel, M.-T. Sougrati, T. Mineva, L. Stievano, E. Fonda and F. Jaouen, Identification of catalytic sites for oxygen reduction in iron- and nitrogen-doped graphene materials, *Nat. Mater.*, 2015, **14**(9), 937–942.

42 X. Wan, Q. Liu, J. Liu, S. Liu, X. Liu, L. Zheng, J. Shang, R. Yu and J. Shui, Iron atom–cluster interactions increase activity and improve durability in Fe–N–C fuel cells, *Nat. Commun.*, 2022, **13**(1), 2963.

43 P. Rao, D. Wu, T.-J. Wang, J. Li, P. Deng, Q. Chen, Y. Shen, Y. Chen and X. Tian, Single atomic cobalt electrocatalyst for efficient oxygen reduction reaction, *eScience*, 2022, **2**(4), 399–404.

44 A. Poerwoprajitno, L. Gloag, J. Watt, S. Cheong, A. Henson, B. Subhash, N. Bedford, B. Miller, P. O'Mara, T. Benedetti, D. Huber, J. Gooding, W. Schuhmann and R. Tilley, A single-Pt-atom-on-Ru-nanoparticle electrocatalyst for CO-resilient methanol oxidation, *Nat. Catal.*, 2022, **5**, 231–237.

45 D. F. van der Vliet, C. Wang, D. Li, A. P. Paulikas, J. Greeley, R. B. Rankin, D. Strmcnik, D. Tripkovic, N. M. Markovic and V. R. Stamenkovic, Unique Electrochemical Adsorption Properties of Pt-Skin Surfaces, *Angew. Chem., Int. Ed.*, 2012, **51**(13), 3139–3142.

46 J. Liu, M. Jiao, L. Lu, H. M. Barkholtz, Y. Li, Y. Wang, L. Jiang, Z. Wu, D.-j. Liu, L. Zhuang, C. Ma, J. Zeng, B. Zhang, D. Su, P. Song, W. Xing, W. Xu, Y. Wang, Z. Jiang and G. Sun, High performance platinum single atom electrocatalyst for oxygen reduction reaction, *Nat. Commun.*, 2017, **8**(1), 15938.

47 W. Liao, S. Zhou, Z. Wang, J. Long, M. Chen, Q. Zhou and Q. Wang, Stress induced to shrink ZIF-8 derived hollow Fe–NC supports synergizes with Pt nanoparticles to promote oxygen reduction electrocatalysis, *J. Mater. Chem. A*, 2022, **10**(40), 21416–21421.

48 P. Sabhapathy, P. Raghunath, A. Sabbah, I. Shown, K. S. Bayikadi, R.-K. Xie, V. Krishnamoorthy, M.-C. Lin, K.-H. Chen and L.-C. Chen, Axial Chlorine Induced Electron Delocalization in Atomically Dispersed FeN_4 Electrocatalyst for Oxygen Reduction Reaction with Improved Hydrogen Peroxide Tolerance, *Small*, 2023, **19**(45), 2303598.

49 Y. Shan, X. Zhang, G. Liu, J. Li, Y. Liu, J. Wang and D. Chen, The Cyanations with Isocyanides: Recent Advances and Perspectives, *Chem. Commun.*, 2024, **60**, 1546–1562.

50 H. Yang, Y. Ko, W. Lee, A. Züttel and W. Kim, Nitrogen-doped carbon black supported Pt–M (M = Pd, Fe, Ni) alloy catalysts for oxygen reduction reaction in proton exchange membrane fuel cell, *Mater. Today Energy*, 2019, **13**, 374–381.

51 X. Zhao, J. Chen, Z. Bi, S. Chen, L. Feng, X. Zhou, H. Zhang, Y. Zhou, T. Wågberg and G. Hu, Electron Modulation and Morphology Engineering Jointly Accelerate Oxygen Reaction to Enhance Zn–Air Battery Performance, *Adv. Sci.*, 2023, **10**(8), 2205889.

52 E. Sanville, S. D. Kenny, R. Smith and G. Henkelman, Improved grid-based algorithm for Bader charge allocation. Markovic, *Nat. Mater.*, 2007, **28**(5), 899–908.

53 J. Zhang, J. Chen, Y. Luo, Y. Chen, Y. Luo, C. Zhang, Y. Xue, H. Liu, G. Wang and R. Wang, A defect-driven atomically dispersed Fe–N–C electrocatalyst for bifunctional oxygen electrocatalytic activity in Zn–air batteries, *J. Mater. Chem. A*, 2021, **9**(9), 5556–5565.

54 Y. Dai, B. Liu, Z. Zhang, P. Guo, C. Liu, Y. Zhang, L. Zhao and Z. Wang, Tailoring the d-Orbital Splitting Manner of Single Atomic Sites for Enhanced Oxygen Reduction, *Adv. Mater.*, 2023, **35**(14), 2210757.

55 C. Jin, J. Li, K. Zhang, Habibullah, G. Xia, C. Wu, Y. Wang, W. Cen, Y. Chen and Y. Yan, Pd_3P nanoparticles decorated

Open Access Article. Published on 08 July 2024. Downloaded on 4/2/2026 6:00:46 PM.
This article is licensed under a Creative Commons Attribution-NonCommercial 3.0 Unported Licence.

P-doped graphene for high hydrogen storage capacity and stable hydrogen adsorption-desorption performance, *Nano Energy*, 2022, **99**, 107360.

56 M. J. S. Dewar and W. Thiel, Ground states of molecules. MNDO results for molecules containing hydrogen, carbon, nitrogen, and oxygen, *J. Am. Chem. Soc.*, 1977, **99**(15), 4907–4917.

57 K. Liu, J. Fu, Y. Lin, T. Luo, G. Ni, H. Li, Z. Lin and M. Liu, Insights into the activity of single-atom Fe–N–C catalysts for oxygen reduction reaction, *Nat. Commun.*, 2022, **13**(1), 2075.

58 R. Venegas, F. J. Recio, J. Riquelme, K. Neira, J. F. Marco, I. Ponce, J. H. Zagal and F. Tasca, Biomimetic reduction of O_2 in an acid medium on iron phthalocyanines axially coordinated to pyridine anchored on carbon nanotubes, *J. Mater. Chem. A*, 2017, **5**(24), 12054–12059.

59 L. Chong, J. Wen, J. Kubal, F. G. Sen, J. Zou, J. Greeley, M. Chan, H. Barkholtz, W. Ding and D.-J. Liu, Ultralow-loading platinum–cobalt fuel cell catalysts derived from imidazolate frameworks, *Science*, 2018, **362**(6420), 1276–1281.

60 L. Huang, Y. Q. Su, R. Qi, D. Dang, Y. Qin, S. Xi, S. Zaman, B. You, S. Ding and B. Xia, Boosting oxygen reduction *via* integrated construction and synergistic catalysis of porous platinum alloy and defective graphitic carbon, *Angew. Chem., Int. Ed.*, 2021, **60**, 25530–25537.

61 B. Hammer and J. K. Nørskov, Electronic factors determining the reactivity of metal surfaces, *Surf. Sci.*, 1995, **343**(3), 211–220.

62 Y. Cheng, X. Gong, S. Tao, L. Hu, W. Zhu, M. Wang, J. Shi, F. Liao, H. Geng and M. Shao, Mechano-thermal milling synthesis of atomically dispersed platinum with spin polarization induced by cobalt atoms towards enhanced oxygen reduction reaction, *Nano Energy*, 2022, **98**, 107341.

63 M. T. Greiner, T. E. Jones, S. Beeg, L. Zwiener, M. Scherzer, F. Girgsdies, S. Piccinin, M. Armbrüster, A. Knop-Gericke and R. Schlögl, Free-atom-liked states in single-atom alloy catalysts, *Nat. Chem.*, 2018, **10**(10), 1008–1015.

64 X. Wang, Y. Li, Y. Wang, H. Zhang, Z. Jin, X. Yang, Z. Shi, L. Liang, Z. Wu, Z. Jiang, W. Zhang, C. Liu, W. Xing and J. Ge, Proton exchange membrane fuel cells powered with both CO and H_2, *Proc. Natl. Acad. Sci. U.S.A.*, 2021, **118**(43), e2107332118.

© 2024 The Author(s). Published by the Royal Society of Chemistry